

# Kinematic State Estimation For A Mars Rover

J. (Bob) Balaram  
Jet Propulsion Laboratory  
California Institute of Technology  
4800 Oak Grove Drive  
Pasadena, California 91109  
USA

## 1 Introduction

Managed for the National Aeronautics and Space Administration (NASA) by the California Institute of Technology, the Jet Propulsion Laboratory (JPL) is the lead United States center for robotic exploration of the solar system. Recently a number of robotic missions to Mars have been undertaken. Mars Global Surveyor is orbiting Mars and sending very high resolution images of the red planet. Mars Pathfinder and its Sojourner Rover have finished their mission after a spectacular landing and the first use of a roving vehicle on Mars.

The Surveyor Program consists of a series of missions that will explore Mars and bring samples to Earth. Current plans call for launching two spacecraft at each launch opportunity every 26 months, typically an orbiter and a lander. The first of these is the '98 mission which will have a lander with a robotic arm. The robotic arm will be used to scoop soil and perform in-situ analysis. In '01 a lander with an arm and a copy of the Sojourner rover is expected to be used for near-lander science operations. The '03 and '05 missions will have long range rovers with several science instruments on-board. These rovers will explore Mars by traversing many kilometers on the surface. In addition they will be drilling rocks and caching samples for return to Earth. The research described in this paper addresses some of the key navigation technologies required to field long range rovers on Mars.

### 1.1 The Sojourner Rover

We briefly summarize the capability of the current state-of-art in planetary rovers by describing the Sojourner rover. This rover has six wheels, each 13 centimeters in diameter and made of aluminum with stainless-steel treads and cleats. A rocker-bogey suspension system allows each wheel to move up and down independently of all the others. Sojourner is capable of scaling a rock of more than 20 centimeters height.

A laser striping system in conjunction with multiple monocular cameras is used to detect obstacles immediately in front of the rover. The vehicle is steered autonomously to avoid obstacles while continuing to attempt to achieve the commanded goal location. Tilt sensors allow the rover to be autonomously halted if it is dangerously close to tipping over.

While stopped, the rover updates its measurement of distance traveled and heading using the averaged wheel odometry and a single on-board heading gyro. This provides an estimate

of progress to the goal location. The lander is also a crucial element for the navigation of the rover. Its stereo cameras obtain panoramic images of the area surrounding the rover which allow mission operators on Earth to periodically locate the rover as well as determine way-points for subsequent rover movements. As a consequence, rover operations are limited to the near vicinity of the lander.

## 1.2 Long Range Rovers

Unlike the Sojourner rover, which traversed a total of 104 meters in the Pathfinder mission, long range rovers could traverse to goals many kilometers from the lander. The scenario for long range rover operations consists of traversing in the commanded direction to a goal region while periodically (e.g., every 100 m to 200 m) transmitting panoramic images to the Earth via a relay satellite. The operators on Earth provide new commands to either continue the traverse, select a new goal, or if the site is of interest to scientists, issue various site survey related commands.

All navigation is without the benefit of a lander and must therefore be highly autonomous. The rover must be able to reliably traverse long distances, avoiding obstacles that are not visible to the operators on Earth in orbiter, lander descent, or lander panoramic images. At a given location, the rover must be able to reliably achieve science goals involving pointing and placement of science instruments on targets designated in returned imagery. Furthermore, the rover should be able to locate itself within the area of operations without the benefit of an external view provided by a lander stereo camera.

In order to achieve these goals, the long range rover research program at JPL has focussed on:

- Implementation of a research rover vehicle called Rocky-7 (the name being derived from the continuing use of the Rocker/Bogey suspension system at JPL).
- Utilizing stereo-imaging to obtain a dense range map of the rover surroundings for use in obstacle avoidance.
- Integrating a celestial sensor (i.e., a sun sensor) to determine the rover's orientation.
- Developing a rover-attached deployable mast with mounted stereo-cameras to obtain high-vantage panoramic images of the area surrounding the rover.
- Developing advanced path-planning techniques in conjunction with mast imagery derived obstacle maps to navigate dense rock fields.
- Utilizing mast imagery derived range maps and range map matching techniques to periodically re-establish the location of the rover within a work area.
- Integrating image feature extraction and tracking methods to serve as a means of visual odometry during rover motion.

- Establishing a state estimation framework to incorporate the information from all of the sensors.

Of these items the last one, namely the state estimation framework, forms the focus of this paper. A key objective is a full state (position and attitude) estimator based on a sensor set consisting of a sun-sensor, gyros, a 3-axis accelerometer and the vehicle kinematic sensors. Of some interest here is to achieve this with a reduction in the electro-mechanical complexity of the vehicle by reducing the the number of gyros to a single heading rate sensor instead of a full 3-axis implementation. The aim is to improve the precision of the odometry estimate by using the full kinematics of the rocker/bogey mechanisms of the rover as it traverses undulating/bumpy terrain. This is considerably more complex than a kinematically simpler vehicle operating on a flat indoor environment.

In addition to providing a backup to vision-based methods in regions of low visual content, improving the precision of the odometry allows vision-based estimation techniques to be improved. Visual feature tracking and range map matching methods can be layered on top of the baseline estimator with increased robustness to failure, reduced search/computation costs, and less frequent use of mast deployments and related imaging operations. The Kalman filtering framework adopted also provides a natural Bayesian means of combining these visually based estimates into the full state estimate. Another objective, is to develop a sensing/estimation framework in which sensors can be enabled/disabled based on monitoring of filter residuals, and mode switching between different estimator banks is triggered by observability conditions.

### 1.3 The Rocky-7 Research Platform

In this section we describe the Rocky-7 rover configuration shown in Figure 1, and detail the components relevant to the navigation of the vehicle.

Like Sojourner, the wheel diameter of Rocky-7 is 13 cm. The mobility system is a modification of the Rocker-Bogey design used in previous rovers at JPL . It consists of two rockers hinged to the sides of the main body. Each rocker has a steerable wheel at one end and a smaller bogey at the other end. Unlike its predecessors Rocky-3 and Rocky-4 (and the Sojourner flight rover) that have four steerable wheels, Rocky-7 has only two. Here too the emphasis is on investigating reduced number of actuators to minimize system electro-mechanical complexity.

The sun-sensor used on Rocky-7 is the Lockheed-Martin Wide Angle Sun Sensor (WASS) with a 160 degree field-of-view providing sun azimuth and elevation in its coordinate frame. It is mounted on the solar panel of Rocky-7. The rate gyro is the QRS-11 vibratory gyro from Systron-Donner, and the accelerometers are from Lucas-Shaevitz mounted in a 3-axis cage. Internal angles of the rover mechanism are read by potentiometers. Wheel drive and steering angles are read by optical encoders.

The rover is equipped with seven CCD cameras, two at each end, for the hazard avoidance system and three on the mast (2 for stereo, and 1 for close-up viewing). The hazard avoidance

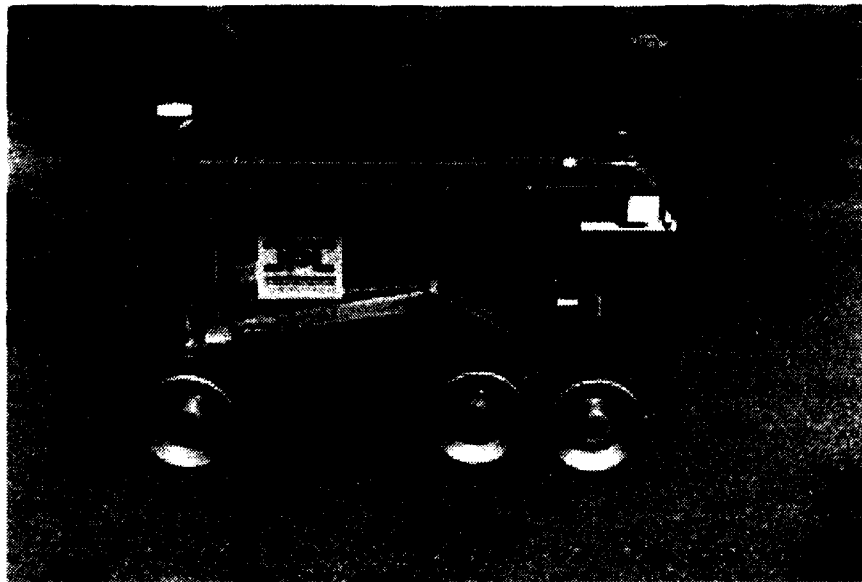


Figure 1: Rocky-7 Side View

system uses passive stereo-vision with a pair of cameras with wide-angle lenses that allow detection of rocks and other hazards extending from near the rover wheels to about 1.5 meters distance.

#### 1.4 Previous Rover State Estimation Work

We briefly describe some representative related work in the area of mobile robot state estimation. Since Global Positioning System (GPS) based methods are not currently applicable to a vehicle on Mars, we have excluded them from our discussion.

A number of efforts have concentrated on the localization of the mobile robot based on external sensor cues. For example, beacon-based localization of a mobile robot has been considered by Leonard [9] in which an Extended Kalman Filter (EKF) is employed to match environment observations to a map. Matthies [11] used a Kalman Filtering approach to track stereo vision features and obtain vehicle motion. Baumgartner and Skaar [2] estimate a vehicle's position and orientation based on visual cues in discrete locations within a structured environment combined with sensed wheel estimates by an EKF. Olson [15] utilizes range map matching to periodically localize a mobile vehicle.

Other efforts have aimed at fusing inertial navigation sensors with odometry. Borenstein and Feng [3] develop a technique called gyrodometry where gyro data is only used when the gyro and odometry estimates differ, such as when traversing a bump. Barshan and Durrant-Whyte [1] also use inertial sensors in an EKF to estimate position. Vaganay and Aldon [17] utilize accelerometers and gyros for vehicle attitude estimation. Fuke and Krotkov [5] utilize gyros and accelerometers together with odometry to estimate vehicle attitude estimates. Their filter allows the accelerometer signal to dominate at low frequencies and the gyro to dominate at higher frequencies. The combination of gyro and sun-sensor data for vehicle

attitude estimation is addressed by Roumeliotis and Bekey [16].

Kinematic techniques include an effort by Kim, et.al [8] to extend a dead-reckoning formula for a two-wheeled mobile robot motion on a known curved surface. Slip modeling for a vehicle operating in the plane is considered by Madhavan, et. al [10]. Here a random walk model for a slip angle parameter is introduced for estimating the motion of a truck with planar articulation elements.

As we see, many vehicle state estimation methods have been applied to vehicles with relatively simple kinematics and no slip, operating on mostly flat terrain, and using expensive external sensor cues such as that provided by vision. In this paper, we attempt to develop new techniques suitable for use on kinematically complex vehicles traversing highly uneven terrain, with explicit modeling of slip, and using a minimal complement of basic sensors.

## 2 Rover Kinematics Model

In this section, we discuss the model used for rover state estimation. This consists of a simple state-space model to smoothly propagate rover position and attitude, a rover kinematic contact model to describe wheel interactions with the ground, and measurement models for the various sensors.

### 2.1 Coordinate Frames and Variables

Coordinate frames and variables are as defined in Figure 2. The unconstrained rover's degrees-of-freedom (dof's) are seen to be three translational, three rotational, three internal ( $\gamma_0, \gamma_1, \gamma_2$ ), two steering ( $\lambda_1, \lambda_2$ ), and six drive ( $\psi_1, \dots, \psi_6$ ). Contact interactions at each wheel constrain these dof's to result in the rover typically having two translational dof's (x,y) and one angular dof (heading) when in full contact with the ground.

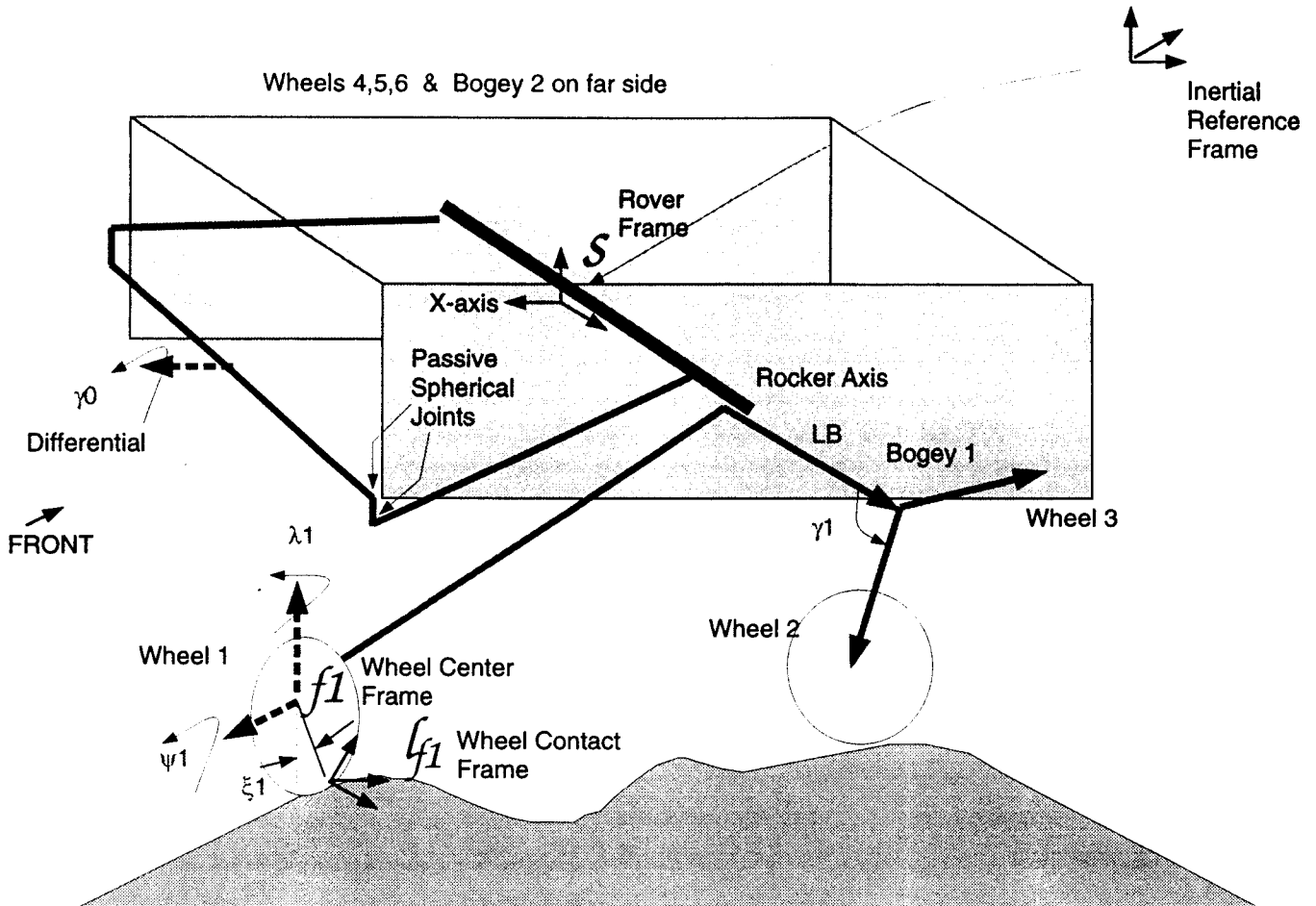


Figure 2: Rocky-7 Kinematics

## 2.2 Process Model

The process model sets up the differential equations governing the system. It defines the state vector and associated state equations.

### 2.2.1 Translation State Equation

A simple kinematic model is provided for the translation of the system.

$$\begin{bmatrix} {}^I \dot{x} \\ \dot{v}_p \end{bmatrix} = \begin{bmatrix} R(q)(v_c + v_p) \\ A_v v_p \end{bmatrix} + \begin{bmatrix} 0 \\ n_v \end{bmatrix} \quad (1)$$

The translational position  ${}^I x \in R^3$ , of the rover frame is resolved in the inertial frame. However, the velocities  $v_c, v_p \in R^3$  are resolved in the body frame. The body velocity  $v$ , is given by the sum of two velocity terms  $v = v_c + v_p$ . The  $v_c$  is the prescribed velocity

that the rover is attempting to follow as generated by the on-board controller. Typically this would be the  $x$  and  $y$  components of the body translational velocity. The  $v_p$  represents a perturbation velocity which is damped out by the damping matrix  $A_v$  and driven by an acceleration noise  $n_v$ . The matrix  $R(q)$  is the rotation matrix of the rover attitude as a function of  $q$ , the attitude quaternion.

### 2.2.2 Attitude State Equation

A purely kinematic model is also provided for the attitude of the system.

$$\begin{bmatrix} \dot{q} \\ \dot{\omega}_p \end{bmatrix} = \begin{bmatrix} \frac{1}{2}\Omega(\omega_c + \omega_p)q \\ A_\omega\omega_p \end{bmatrix} + \begin{bmatrix} 0 \\ n_\omega \end{bmatrix} \quad (2)$$

All angular variables are resolved in body coordinate with  $q \in R^4$  being the attitude quaternion. The total body angular velocity  $\omega$  is the sum of two terms  $\omega = \omega_c + \omega_p$ , with  $\omega_c, \omega_p \in R^3$ . The  $\omega_c$  is the prescribed rate that the rover is attempting to follow as generated by the on-board controller. Typically this would be the  $z$ -axis component of the body angular velocity. The  $\omega_p$  then represents a perturbation angular velocity which is damped out by the damping matrix  $A_\omega$  and driven by an angular acceleration noise  $n_\omega$ . The terms in quaternion evolution equation are given by:

$$\Omega(\omega) \triangleq \begin{bmatrix} -\omega^\times & \omega \\ -\omega^T & 0 \end{bmatrix}; \quad \omega^\times \triangleq \begin{bmatrix} 0 & -\omega_3 & \omega_2 \\ \omega_3 & 0 & -\omega_1 \\ -\omega_2 & \omega_1 & 0 \end{bmatrix} \quad (3)$$

### Small Angle Evolution

The basic idea is to define an intermediate local model to which the standard continuous-discrete Extended Kalman Filter (EKF) equations can be applied [6]. Let the quaternion  $q$  be given in terms of angle/axis variables  $(\Theta, u)$ , where  $\Theta \in \mathcal{R}^1$  and unit vector  $u \in \mathcal{R}^3$ , as [7]:

$$q = \begin{bmatrix} \epsilon \\ \eta \end{bmatrix} \quad (4a)$$

$$\epsilon = u \sin(\Theta/2) \quad (4b)$$

$$\eta = \cos(\Theta/2) \quad (4c)$$

Because the normalization constraint  $q^T q = 1$  is not explicitly enforced in the estimator design, the quaternion  $q$  acts as an over-parameterized representation of the 3-axis attitude. In order to avoid the redundant state, a local vector angular variable  $\theta \in \mathcal{R}^3$  is defined by

a local linearization at the beginning of each propagation step. After the completion of the corresponding update step, the local angular variable is absorbed into the quaternion from the previous linearization. The process is continued with subsequent linearizations. The corresponding covariance terms are maintained in terms of the local angular variable, which characterizes a ball of uncertainty about the attitude estimate.

For some  $t = t_0$  and  $q(t_0) = q_0$ , a local angular variable  $\theta$  is defined by the change of variables:

$$q(t) = q_0 \begin{bmatrix} \theta(t)/2 \\ 1 \end{bmatrix} \quad (5)$$

which can be solved to give:

$$\theta(t) = 2Im\{q_0^* q\} \quad (6)$$

where “ $Im\{.\}$ ” is used to indicate the first three so-called imaginary components of the quaternion as given in (4a). Then from (2) and (3) the linearized equation for  $\theta$  becomes:

$$\dot{\theta} = \omega - \frac{1}{2} \omega^\times \theta = (\omega_c + \omega_p) - \frac{1}{2} (\omega_c^\times + \omega_p^\times) \theta \quad (7)$$

Note that this parameterization is linear in  $\theta$  but preserves the nonlinear dependence of  $\omega$  for this accuracy in  $\theta$ . This is a locally valid nonlinear system which avoids difficulties associated with the redundancy of a quaternion representation of attitude. However, it is nonlinear and remains to be *further* linearized in the usual EKF sense to realize the propagation and update stages of the filter.

### 2.2.3 Contact State Equation

$$\begin{bmatrix} \dot{\xi} \end{bmatrix} = \begin{bmatrix} A_\xi \xi \end{bmatrix} + \begin{bmatrix} n_\xi \end{bmatrix} \quad (8)$$

The contact point vector  $\xi = \{\xi_1, \xi_2, \xi_3, \xi_4, \xi_5, \xi_6\}$  is modeled very simply as a set of one parameter contacts about the equator of each wheel, with the nominal contact position  $\xi_i = 0$ . In reality there is an additional off-equatorial coordinate for the contact point at each wheel, a contact rotation angle, and two parameters that describe the point on the ground [13]. However the one parameter model suffices to capture and couple the rotational and translational velocities. The dynamics of  $\xi$  encoded in  $A_\xi$  ensure that the contact point eventually returns to the nominal position and thereby ensures correct steady-state behavior in the estimator when the rover travels on slopes of constant inclination.

There are issues regarding the observability of the contact points which are not discussed here. However, the experimental results indicate generally good observability for typical rover motions.

## 2.2.4 Gyro Bias State Equation

$$[ \dot{b} ] = [ n_b ] \quad (9)$$

The gyro bias vector  $b = \{b_1, b_2, b_3\}$  is modeled as a random-walk. Normally, the periodic measurement of all three attitude components by an absolute sensor such as 3-angle sun-sensor allows the gyro biases to be estimated while the rover is in motion. However, if only a single gyro is used in conjunction with a sun-sensor that only measures 2 attitude variables, then gyro bias observability is more complex, becoming a function of the sun-angle geometry and the kinds of attitude motions being undertaken by the rover. However, since the Mars rover operations call for the rover to periodically come to a stop (every few meters), bias can be simply estimated by averaging the gyro data during these times when the rover is stopped. Therefore we choose to not incorporate this model into the state estimator at this time.

## 2.3 Measurement Model

The measurement models relate the state variables to the sensor data available from the system. Here we consider the standard complement of sensors available to the rover, as well as a kinematic constraint that we treat as a measurement.

### 2.3.1 Accelerometer Equation

The accelerometer readings is given by:

$$[ a_m ] = [ a + \omega^\times v - R^T(q)g + \omega^\times \omega^\times L^b + \dot{\omega}^\times L^b ] + [ n_a ] \quad (10)$$

Here all variables are resolved in body coordinates and the accelerometer frame is assumed to be aligned with the rover frame. The term  $L^b$  is the vector from the rover frame to the accelerometer frame origin. If the acceleration  $a$  is not modeled as a state, then the accelerometer data can be used to drive the process equation in the so-called *sensor integrating form* in lieu of the expression in Equation 1:

$$\dot{v}_p = a_m - \dot{v}_c + R^T(q)g - (\omega^\times v_p + \omega^\times v_c + \omega^\times \omega^\times L^b + \dot{\omega}^\times L^b) \quad (11)$$

### 2.3.2 Gyro Equation

$$[ \omega_m ] = [ B_g \omega + b ] + [ n_g ] \quad (12)$$

Here the gyro measurement  $\omega_m$  gives the angular rate  $\omega$  in the body frame. If a full 3-axis gyro is present the  $B_g$  is an Identity matrix. However, if only a heading gyro is present, the matrix  $B_g$  implements the one-axis gyro measurement with:

$$B_g \triangleq \begin{bmatrix} 0 & 0 & 1 \end{bmatrix} \quad (13)$$

### 2.3.3 Sun-Sensor Equation

The sun-sensor design is a wide-angle lens which projects an image of the sky on a two-dimensional position sensing device [4]. The output currents of this device, specifically the ratio of currents for each dimension, provides the position of the centroid of the Sun's image from the edge of the device. With the edge currents designated as  $\{I_1, I_2, I_3, I_4\}$  the centroid location is given by:

$$s_m(1) = \frac{(I_1 + I_4) - (I_2 + I_3)}{I_1 + I_2 + I_3 + I_4} \quad (14a)$$

$$s_m(2) = \frac{(I_1 + I_2) - (I_3 + I_4)}{I_1 + I_2 + I_3 + I_4} \quad (14b)$$

The sun-sensor has optics most easily described by a fish-eye lens model. In the sun-sensor frame, the sun azimuth angle is given by  $\text{atan}(s_m(2), -s_m(1))$ , and elevation by  $\pi/2(1 - \sqrt{s_m(1)^2 + s_m(2)^2})$ . Equivalently, we choose to consider the output of the sensor to be a function of the two independent components of the unit vector to the sun as resolved in the sun-sensor frame. This is given by:

$$\begin{bmatrix} s_m \end{bmatrix} = (2/\pi) \frac{\arcsin(\sqrt{s_x^2 + s_y^2})}{\sqrt{s_x^2 + s_y^2}} \begin{bmatrix} s_x \\ s_y \end{bmatrix} + \begin{bmatrix} n_s \end{bmatrix} \quad (15)$$

where:

$$\begin{bmatrix} s_x \\ s_y \end{bmatrix} = \begin{bmatrix} 1 & 0 & 0 \\ 0 & 1 & 0 \end{bmatrix} R^T(q) s_v \quad (16)$$

The unit vector  $s_v$  represents the sun-vector in inertial coordinates. This vector is rotated into the sun-sensor coordinate system (which is taken to be the rover frame) by the matrix  $R(q) \in R^{3 \times 3}$  corresponding to the quaternion  $q$ . The noise term  $n_s$  lumps the effects of electronics noise as well as calibration errors.

### 2.3.4 Kinematic Slip Equation

There is no simple analytical formulation of the inverse kinematics map that relates wheel rotations and contact interactions to the vehicle motion. Such a map must necessarily involve

the dynamics of the vehicle and is too complicated for implementation in the filter. Instead we choose to embed the easily established forward kinematics within a *measurement* in the filter. We shall see that this allows a natural implementation of the full kinematics of the vehicle. It exploits the ability of the Kalman filter to perform the appropriate least-squares averaging of the action of each kinematic chain in the rover.

Each such forward kinematic chain has a component defined by sequence of links joining the rover frame to each wheel contact point, and a component given by the slip between the wheel and the ground. We introduce the notion of a slip measurement,  $t_{m_i}$ , that defines the relative 6-dof motion of the contact frame  $l_{f_i}$  (see Figure 2) on the wheel with respect to the ground. This slip is a function of the vehicle configuration, the 6-dof vehicle velocity, the wheel-to-ground contact point location, and the joint rates associated with the kinematic chain emanating from the rover frame to the contact point.

$$t_{m_i} = B^T Ad_{g_{sl_{f_i}}}^{-1}(\gamma, \lambda, \xi_i) \left( \begin{bmatrix} v_c + v_p \\ \omega_c + \omega_p \end{bmatrix} + J_{s_{f_i}}^s(\gamma, \lambda) \begin{bmatrix} \dot{\gamma} \\ \dot{\lambda} \\ \dot{\psi} \end{bmatrix} \right) + [n_{t_i}] \quad (17)$$

The  $Ad_g^{-1}$  term is the Adjoint Operator [14] given by:

$$Ad_g^{-1} = \begin{bmatrix} R^T & -R^T p^\times \\ 0 & R^T \end{bmatrix} \quad (18)$$

with

$$p^\times \triangleq \begin{bmatrix} 0 & -p_3 & p_2 \\ p_3 & 0 & -p_1 \\ -p_2 & p_1 & 0 \end{bmatrix} \quad (19)$$

The term  $g_{sl_{f_i}}$  represents the transformation from the rover frame to the contact point. The term  $J_{s_{f_i}}^s$  represents the Spatial Jacobian [14] to each wheel center and is a function of the kinematics of the rover.

Here the internal angles are represented by  $\gamma = \{\gamma_0, \gamma_1, \gamma_2\}$ , the steering angles by  $\lambda = \{\lambda_1, \lambda_2\}$ , the drive angles by  $\psi = \{\psi_1, \psi_2, \psi_3, \psi_4, \psi_5, \psi_6\}$ , and the contact point by  $\xi_i$ . The terms  $Ad_g^{-1}$  is a function of  $\gamma$ ,  $\lambda$ , and  $\xi$ . However, it is not a function of the driving angles  $\psi$  because of rotational symmetry of the wheel. The term  $J_{s_{f_i}}^s$  is also not a function of the driving angles  $\psi$  and is only a function of  $\gamma$  and  $\lambda$ .

A variety of choices are possible for the  $B$  matrices. We choose to adopt the  $B$  matrix

for pure rolling as given by:

$$B = \begin{bmatrix} 1 & 0 & 0 & 0 \\ 0 & 1 & 0 & 0 \\ 0 & 0 & 1 & 0 \\ 0 & 0 & 0 & 0 \\ 0 & 0 & 0 & 0 \\ 0 & 0 & 0 & 1 \end{bmatrix} \quad (20)$$

This slip measurement can be decomposed into a known deterministic component and a component that is only known in a statistical sense. The deterministic component of the slip, indicated by a non-zero nominal value of  $t_m$ , is used to capture the effects of a known steering action. For example, a known rotational slip about the vertical is always present at each wheel to accommodate the yaw motion of the vehicle during a turn. Also, some transverse slip is introduced due to the nature of the non-steered bogey wheels on a rover like Rocky-7. In this case, the bogey wheels have their rotation axis on two parallel lines longitudinally ( $\hat{x}$ ) offset from each other. As a consequence there is always some transverse slip even during an Ackerman based steering turn unless one is going on a straight line on flat terrain. These deterministic slips are easy to calculate for Ackerman steered motions on flat ground and are used as approximations to the true deterministic slip even during motion over non-flat terrain. Another deterministic slip measurement can be derived from experiments. For example, over sandy terrain, a known rate of experimentally derived longitudinal ( $x$ ) slip during traverses can be added as a non-zero  $t_m$  term.

A slip action that is only modeled statistically is due to the wheel-ground interaction at each individual wheel. Consider the case when each wheel is driven by a control algorithm that attempts to maximize compliance of the wheel-ground rolling interaction, and also maximally coordinates the control effort across all the wheels. Then the slips at each wheel in the longitudinal ( $x$ ) rolling direction are all independent of each other. In this case of *Uncorrelated Slip Noise*, the slip can be modeled as independent white noise with the corresponding correlation matrix having terms only on the diagonal. Now consider a rover in which each wheel is independently driven by a high-gain, “stiff” control algorithm. Then each wheel rotates to follow the set-point established by the controller and does not accommodate to any wheel-ground forces of interaction. The slips at each wheel are then just direct kinematic transformations of the deviation of the vehicle frame motion from its nominal path. The covariance matrix of this *Correlated Slip Noise* can be derived by transforming the process noise of the vehicle motion by the Jacobian from the vehicle frame to the wheel-to-ground contact frames, and will contain many off-diagonal terms.

Another statistically modeled slip action is due to the terrain curvature. As the vehicle makes progress on the terrain, the rocker-bogey mechanism mostly accommodates the vehicle to maintain contact over the terrain and a highly compliant wheel controller can zero out any rolling slip. However, there is usually some inevitable transverse slip at each wheel to accommodate the curvature changes of the surface at each wheel contact. This slip can be modeled as a zero-mean process with time constants and dynamics related to the rate of change of surface curvature parameters along the rover path.

In actual practice, the slip at the wheel is a combination of all of the above processes. We choose not to model all the statistically describable noise terms in all of their complexity. Instead we select a simple un-correlated slip model for our early implementations, with the covariance strengths determined by experiments. There may also be opportunities to develop a slip related measurement using the motor current data on the drive motors but this too has not been explored in detail yet.

### 3 Nonlinear State Estimation

In this section, a nonlinear state estimation scheme is developed based on the process and measurement models defined in Section 2.2 and Section 2.3.

In this paper, from the various measurement models, we have chosen to focus on those implementing the heading gyro in conjunction with the sun-sensor. We have deliberately not considered the use of 3-axis gyro because of our interest in minimizing the number of attitude sensors used. As the gyro and sun-sensor appear adequate in capturing attitude information we have chosen, at present, to not use the accelerometer measurements. However, they could serve the the purpose of establishing long time-scale attitude variations. It should be noted that the use of the accelerometer data as a sensor for vehicle acceleration is very sensitive to small attitude errors.

We choose to model the various joint angles and corresponding rates as largely deterministic so as to avoid having to introduce these as additional states in the filter. Each of these joint variables is independent of the others and is directly observable from measurements with only some simple smoothing and differencing to derive the corresponding angles and rates.

The Kalman filter state is denoted by

$$X = (\theta, \omega_p, x, v_p, \xi)^T \quad (21)$$

Note that we are using the small-angle process model defined by Equation 7. The measurement vector is denoted by:

$$Y = (\omega_m, s_m, t_m)^T \quad (22)$$

The overall nonlinear state estimation scheme for propagating the state  $X$ , covariance  $P$ , and associated quaternion state  $q$  can be outlined as follows:

1. For given  $X_{k-1}(+)$ ,  $P_{k-1}(+)$ ,  $q_{k-1}(+)$  re-parameterize in terms of the local quaternion state  $q_0 = q_{k-1}(+)$  to get state and measurement equations.
2. Implement standard continuous-discrete EKF algorithm (cf. [6], p. 188).

(i) *Propagate* state and covariance from  $t_{k-1}$  to  $t_k$ :

$$X_{k-1}(+) \rightarrow X_k(-) \quad (23a)$$

$$P_{k-1}(+) \rightarrow P_k(-) \quad (23b)$$

(ii) *Update* state and covariance at  $t_k$ :

$$X_k(-) \rightarrow X_k(+) \quad (24a)$$

$$P_k(-) \rightarrow P_k(+) \quad (24b)$$

3. *Update* associated quaternion state and re-initialize local angular variable at  $t_k$ :

$$q_k(+) = q_{k-1}(+) \begin{bmatrix} \theta_k(+)/2 \\ 1 \end{bmatrix} \quad (25a)$$

$$\theta_k(+) = 0 \quad (25b)$$

4. Proceed to next stage of propagation and updating ( $k \leftarrow k + 1$ ).

## 4 Experiments

Two sources of data are available for validating the state estimation algorithms. The first is test data from Rocky-7 operated in the JPL Mars Yard, a 15 X 25 meter outdoor test area that closely simulates Mars-like terrain constructed on the basis of statistical analysis of images taken by Viking Landers I and II. The second source is a high-fidelity kinematic simulator of the rover contact kinematics [18]. This simulator solves for the contact configuration for a set of closely spaced points along a specified rover path. It then uses the contact geometry and surface parameters of the wheel and ground to derive wheel motion. As such the results correspond closely to the case of highly compliant control algorithm at each wheel minimizing slip in the rolling direction.

We report results for three test setups. The first two are for a simulated Rocky-7 rover where extensive comparisons to the ground-truth data is possible. Then we show some experimental results on the Rocky-7 system with data from the Mars Yard.

### 4.1 Filter Operation With Simulated Data

Here we demonstrate the tracking of rover position and attitude from a combination of sun-sensor, heading gyro and the wheel sensors. Two test cases are simulated. The first one corresponds to the case of a rover moving in a straight line over an undulating terrain. The second test case corresponds to a turn-in-place maneuver over the same terrain. In both

experiments the Sun is assumed to be along the vector  $[-1, 1, 1]/\sqrt{3}$ . The surface is modeled as:

$$z = 0.2 \left( \frac{0.25}{e^{5(6.25(-0.5+x)^2 + 6.25(-0.2+y)^2)}} - \frac{0.25}{e^{4(6.25(-0.5+x)^2 + 6.25(0.2+y)^2)}} + 0.5 \sin(0.75xy) \right) \quad (26)$$

#### 4.1.1 Straight-Line Motion

A sequence of animation cells (left-to-right, top-to-bottom order) in Figure 3 shows the rover motion.

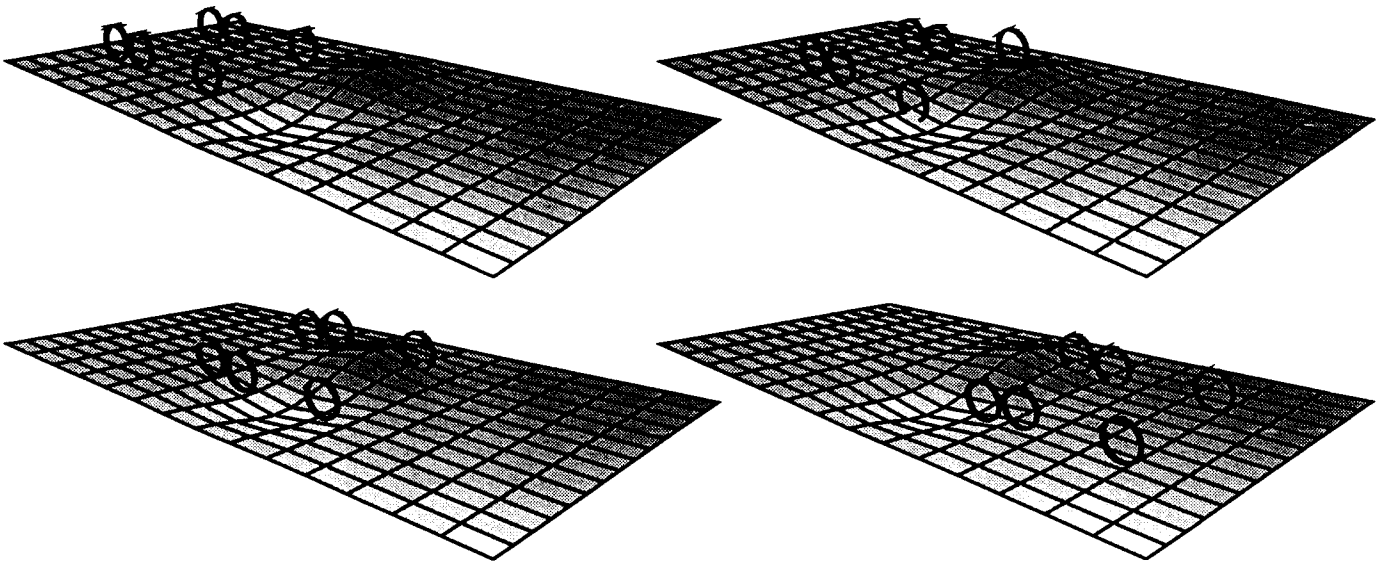


Figure 3: Rocky-7 Straight-Line Motion Over Undulating Terrain

Sensor data is shown in Figures 4, 5, 6, and 7. As the steering angles are fixed during this motion they are not plotted. We also chose to plot the drive joint rates as these highlight the drive variations at each wheel as they move across the surface.

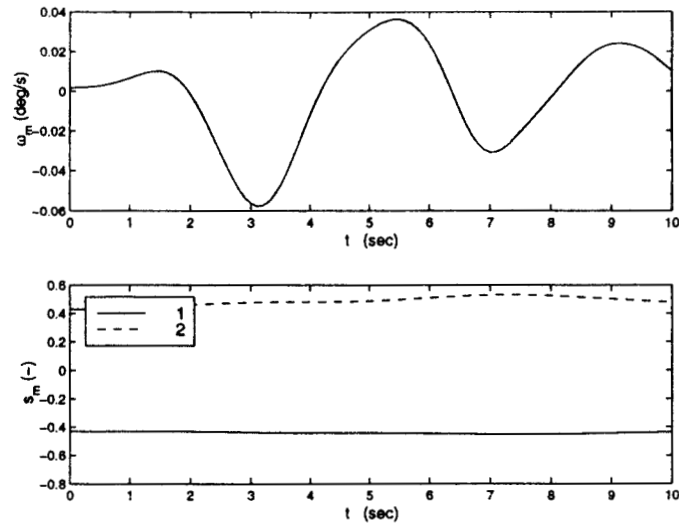


Figure 4: Heading Gyro and Sun-Sensor Data

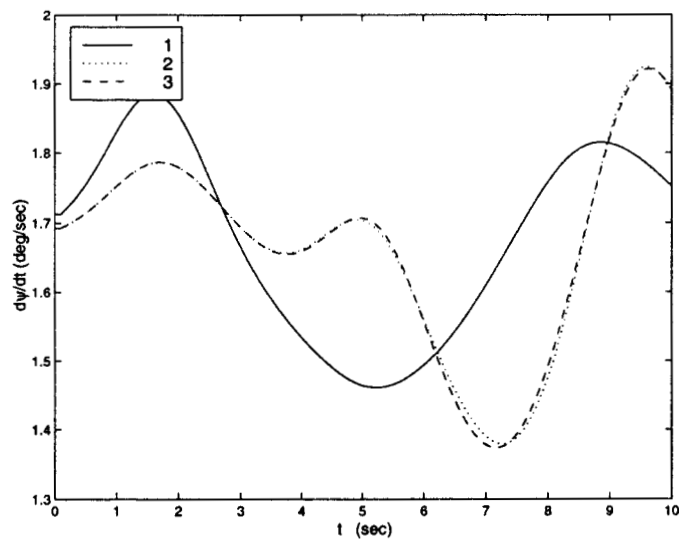


Figure 5: Left Drive Train Rates

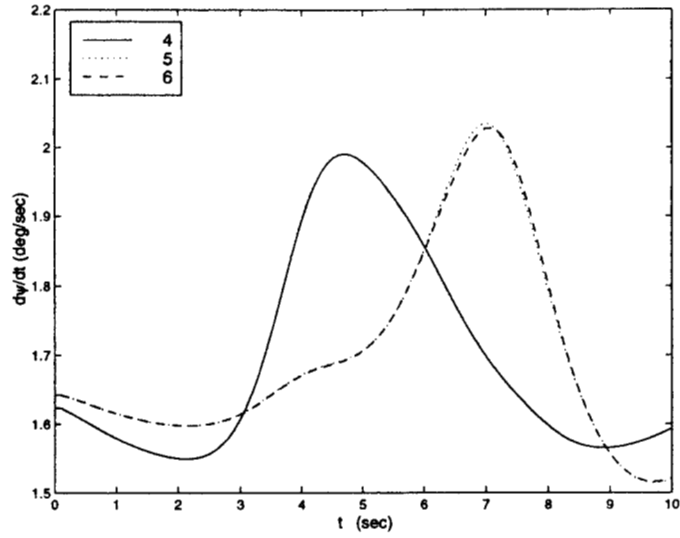


Figure 6: Right Drive Train Rates

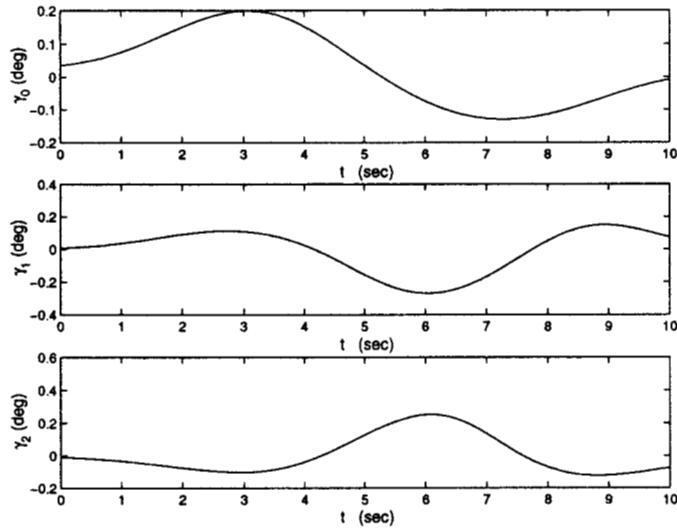


Figure 7: Internal Joint Angles

For the straight-line motion, the ground-truth attitude and the estimated values are shown in Figure 8. The ground-truth position and the estimated values are shown in Figure 9 and the ground-truth contact points and the estimated values are shown in Figure 10.

We note the cross-track error in  $\hat{x}(2)$  reaches a maximum of about 14 mm. This is a result of a one-directional transverse slip active for the portion of the motion shown. Over a larger section of terrain this slip component would average out to zero resulting in the filter reporting only a small cross-track error on average. We also observe that the tracking of the contact points is quite accurate, although with some lag.

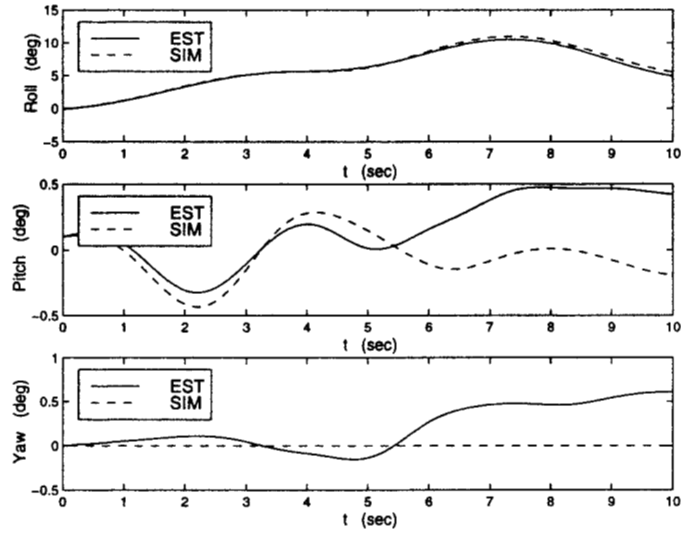


Figure 8: Ground-Truth and Estimate For Attitude

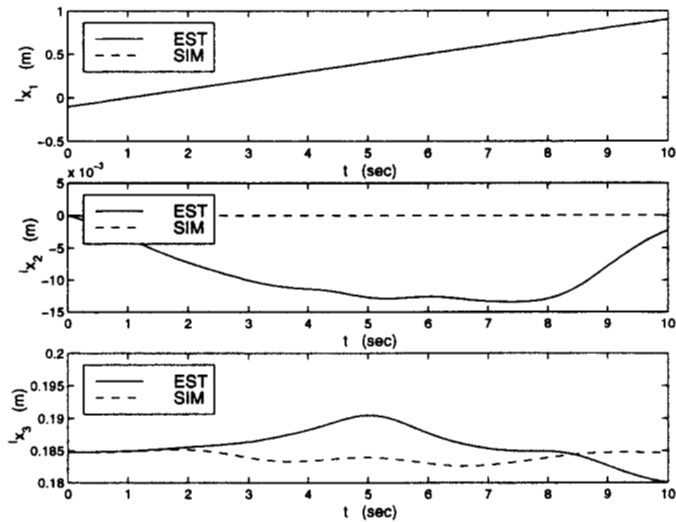


Figure 9: Ground-Truth and Estimate For Position

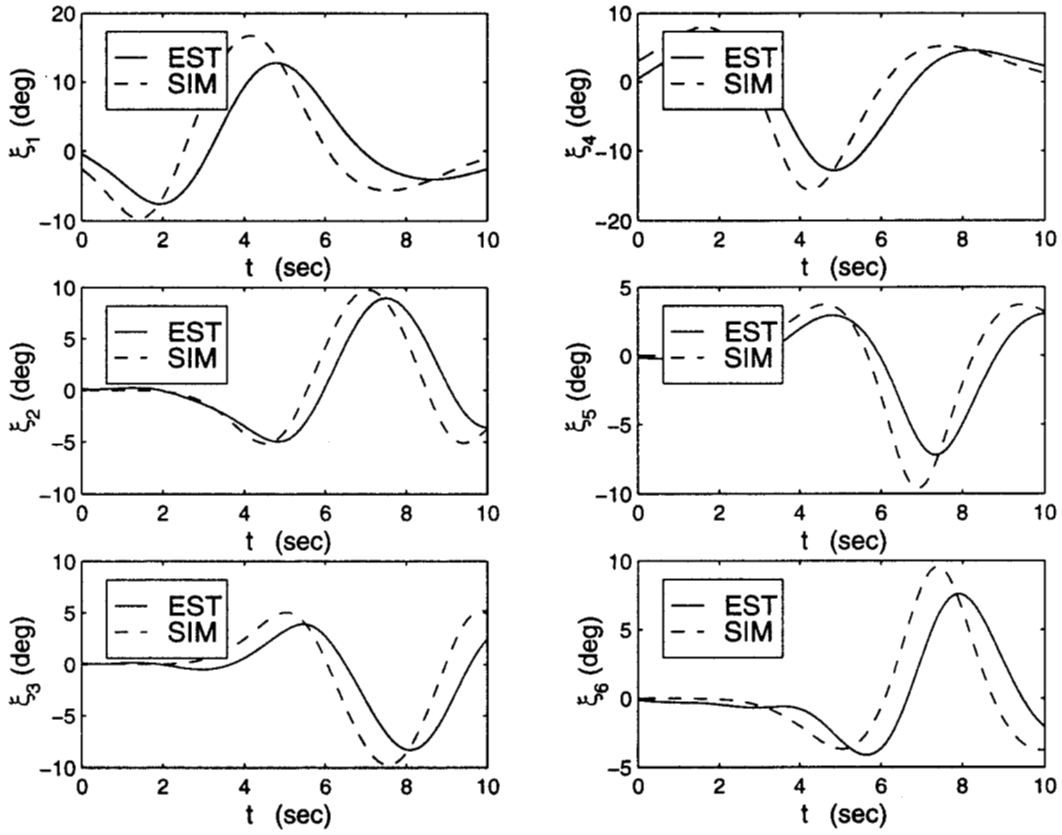


Figure 10: Ground-Truth and Estimate For Contact Points

The corresponding covariances are shown in Figure 11 and Figure 12. As expected there is a growth of the positional covariance with time.

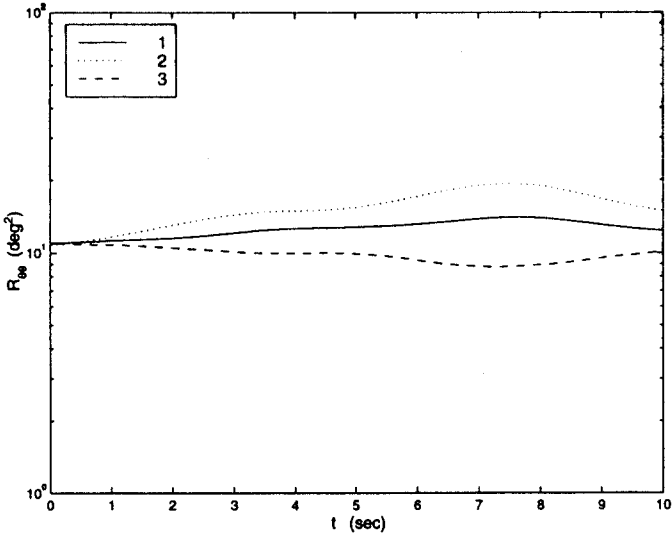


Figure 11: Covariance of Attitude Estimate In Terms of Small Angles

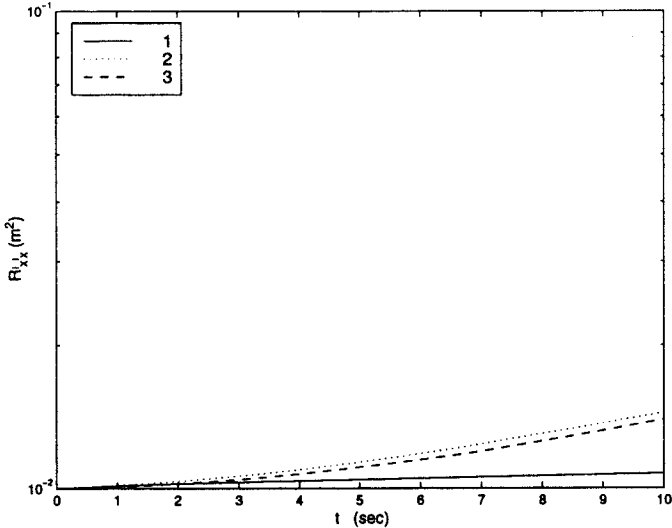


Figure 12: Covariance of Position Estimate

4.1.2 Turn-In-Place Motion

A sequence of animation cells (left-to-right, top-to-bottom order) in Figure 13 shows the turn motion.

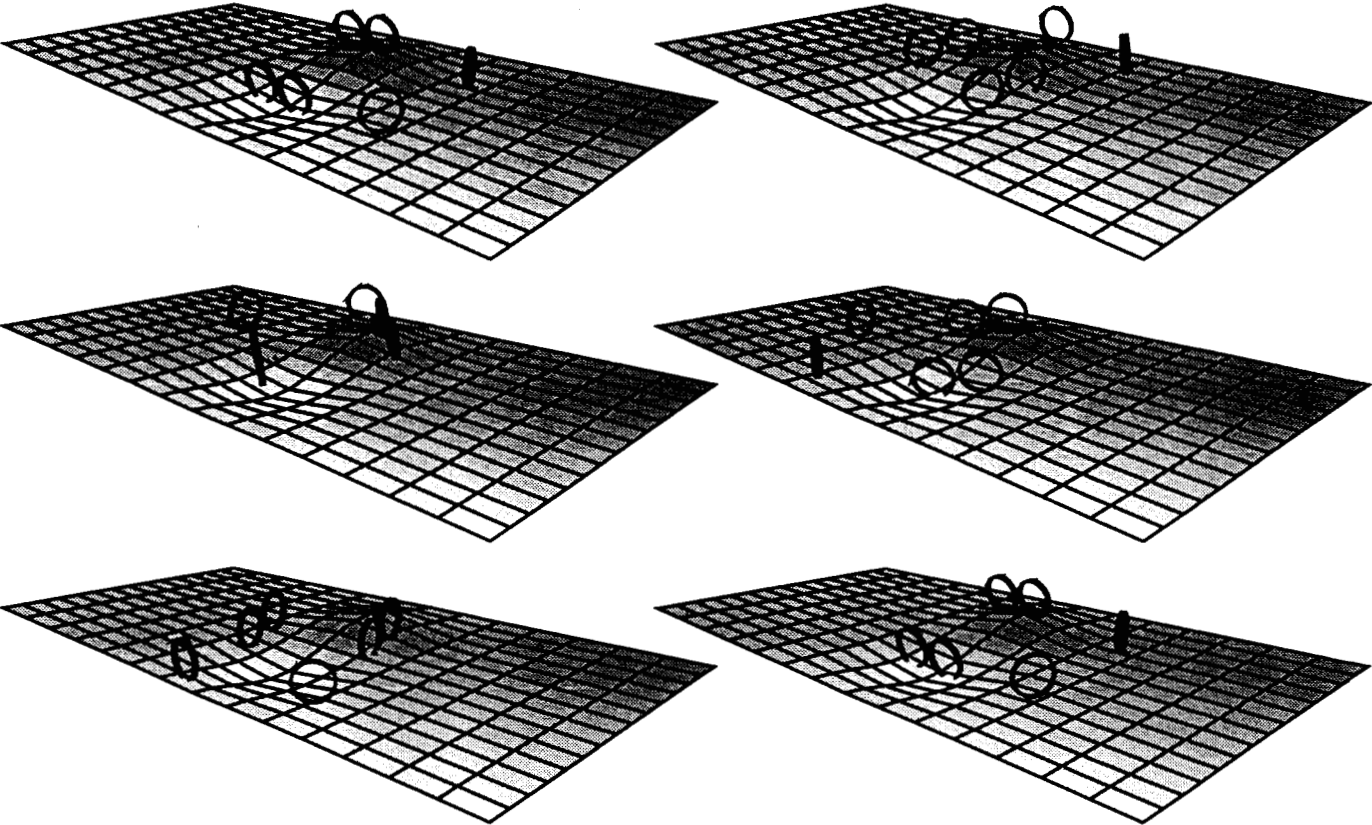


Figure 13: Rocky-7 Turn-In-Place Motion Over Undulating Terrain

As before in the case of straight-line motion, sensor data is shown in Figures 14, 15, 16, and 17.

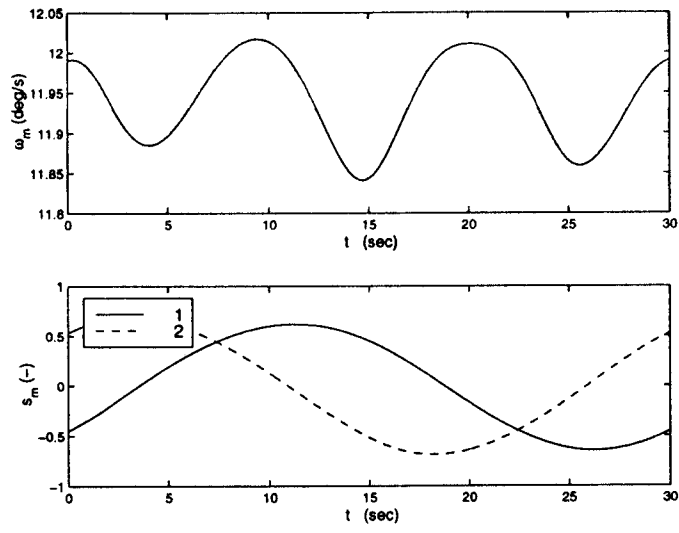


Figure 14: Heading Gyro and Sun-Sensor Data

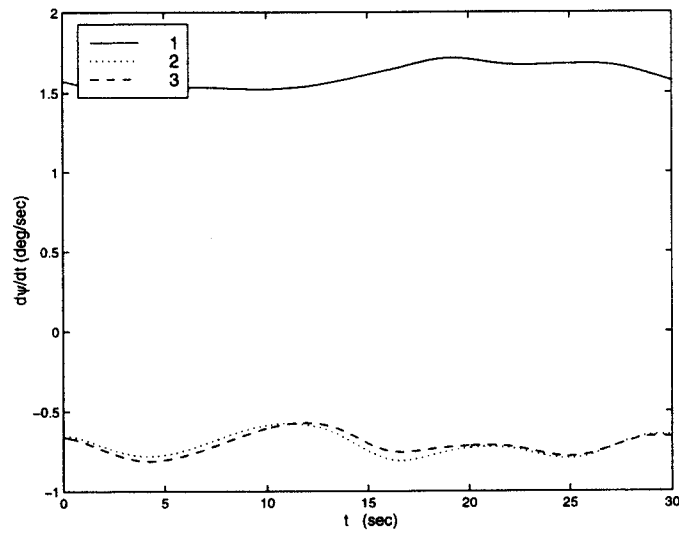


Figure 15: Left Drive Train Rates

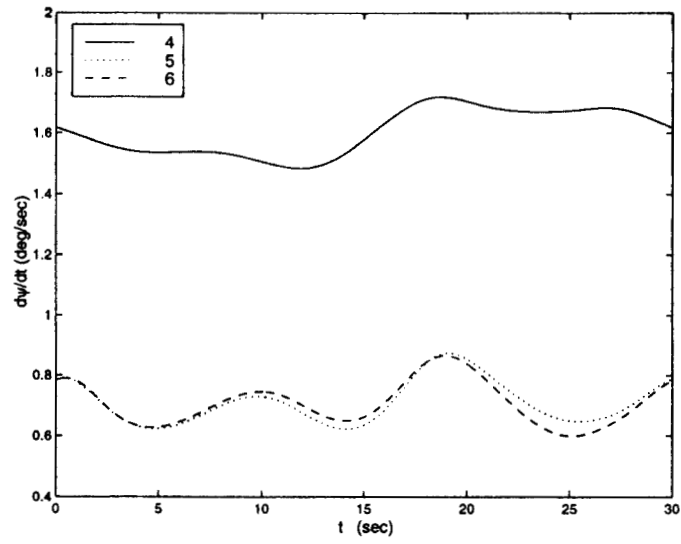


Figure 16: Right Drive Train Rates

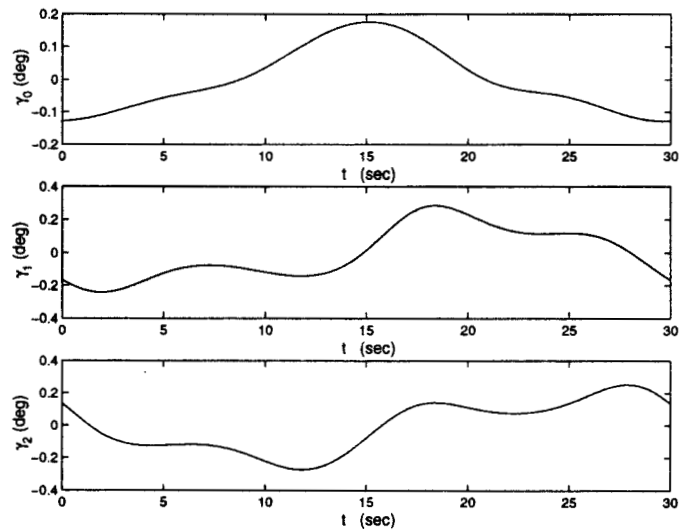


Figure 17: Internal Joint Angles

For the turn-in-place motion, the ground-truth attitude and the estimated values are shown in Figure 18. The ground-truth position and the estimated values are shown in Figure 19 and the ground-truth contact points and the estimated values are shown in Figure 20.

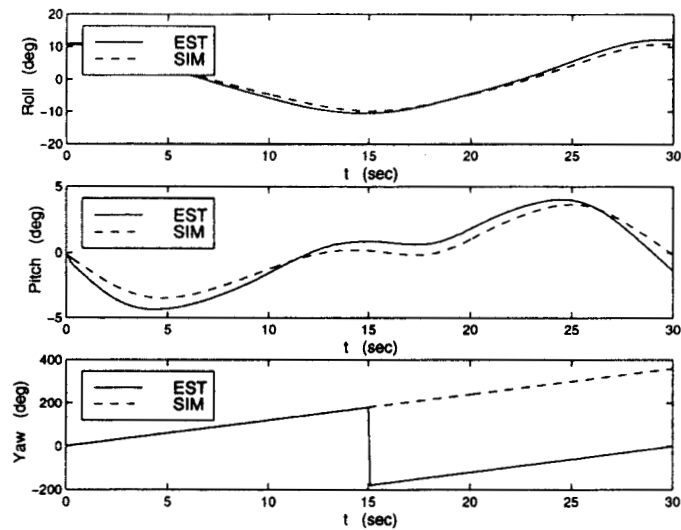


Figure 18: Ground-Truth and Estimate For Attitude

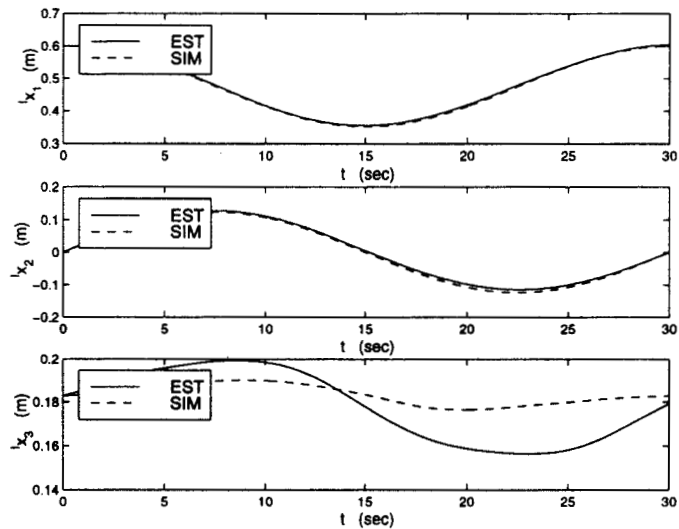


Figure 19: Ground-Truth and Estimate For Position

We note that as the various slip noise values tend to average out to zero as the rover returns to its starting point, the estimates also recover from any bias shown during the motion. We also note that the contact point tracking is quite good except for bogey wheels 3 and 6.

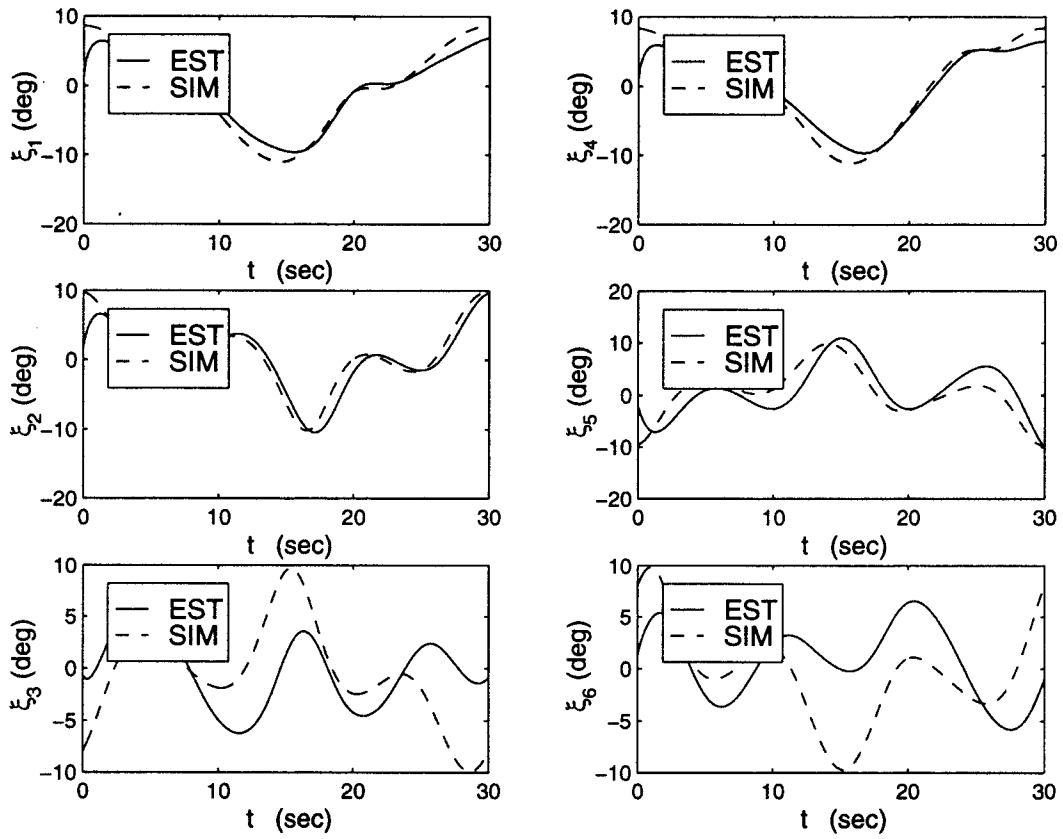


Figure 20: Ground-Truth and Estimate For Contact Points

The corresponding covariances are shown in Figure 21 and Figure 22. As expected there is a growth of the positional covariance with time.

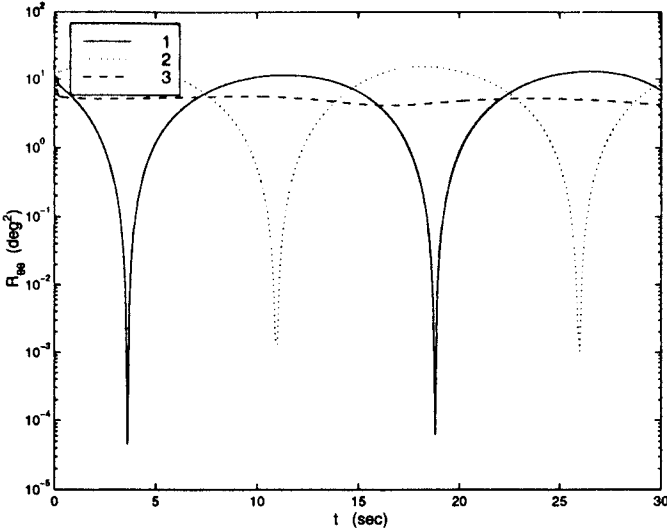


Figure 21: Covariance of Attitude Estimates In Terms of Small Angles

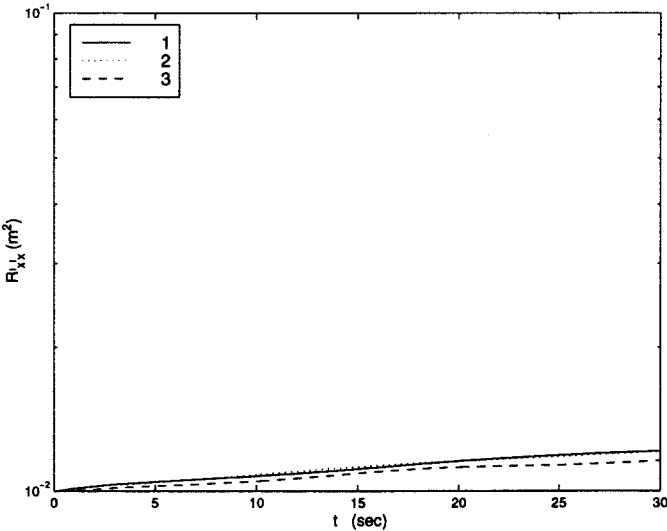


Figure 22: Covariance of Position Estimate

## 4.2 Filter Operation With Experimental Data

Here we demonstrate the tracking of rover position and attitude from a combination of sun-sensor, heading gyro and the wheel sensors. The control algorithm used on the rover consists of individual high-gain controllers on each wheel. No wheel coordination is attempted based on any of the returned sensor data. The motion for this test set consists of a straight-line traverse on flat terrain with a single obstacle (a brick) encountered by the right wheels (wheels 4,5,6). The obstacle is successfully traversed with the rover coming to rest with a portion of the right bogeys (wheels 5,6) still resting on the obstacle.

The obstacle causes two simultaneous effects. It results in a rover pitch-up as the wheels negotiate the obstacle as well as a change in the roll angle. Due to the momentum of the rover motion, there is minimal change in the rover heading. The data set is for a twenty second period with the filter operating at 10 Hz.

Sensor data from the attitude sensors is shown in Figures 23. As the steering angles are fixed during this motion they are not plotted. We also note that due to the nature of the control, all the drive wheels follow essentially the same commanded 5th-order spline trajectory regardless of the forces and torques experienced at each wheel. We have therefore chosen to only plot one of these, namely that for wheel-1 in Figure 24. Internal configuration angles are plotted in Figure 25. In this experimental run, we did not have access to the prescribed motion values being generated by the controller. We therefore treat the entire body velocity of the rover as a perturbation and allow an increased process noise term in the filter to allow for its estimation.

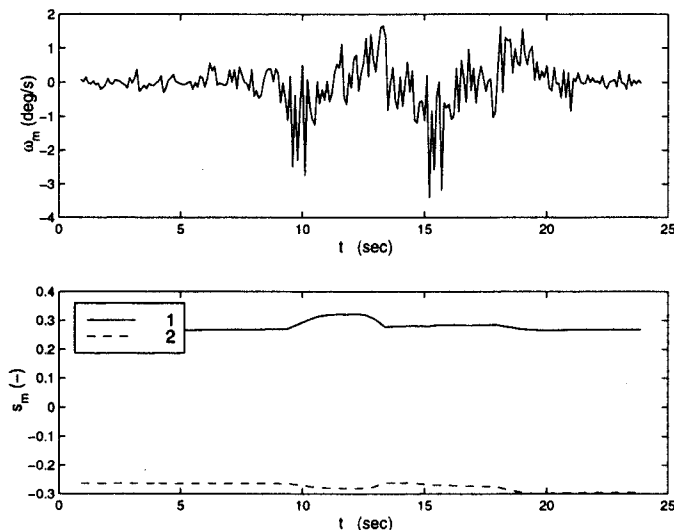


Figure 23: Heading Gyro and Sun-Sensor Data

The estimated angles are shown in Figure 26. We see that the estimator has correctly picked up the roll and pitch deflections induced by the obstacle.

The estimated positions and velocities are shown in Figure 27. We see that the estimator has correctly picked up the z-deflection caused by the brick that results in an

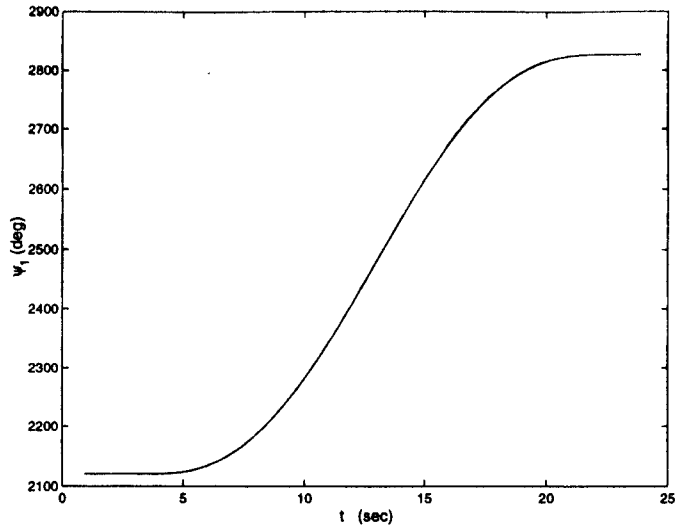


Figure 24: Left Wheel-1 Drive Train Angle

increase in vehicle height.

Estimated contact states are shown in Figure 28. We note that the contact angle variations are quite large under the right wheels as would be expected by the traversal of those wheels over the obstacle. Since the final configuration of the rover is such that the right-side bogey wheels are in the middle of traversing the obstacle, the contact points are significantly displaced from zero. However, the contact point for the right front wheel returns to near zero as it proceeds on level ground after climbing over the obstacle. As expected the wheels on the left side of the vehicle experience very little change in contact angles.

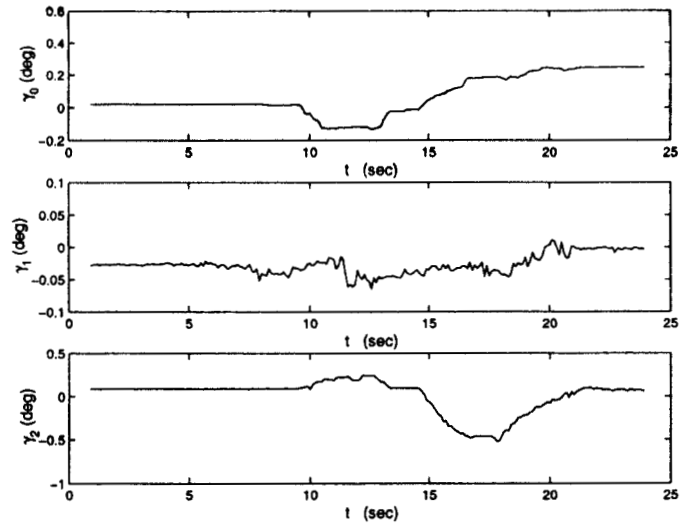


Figure 25: Internal Joint Angles

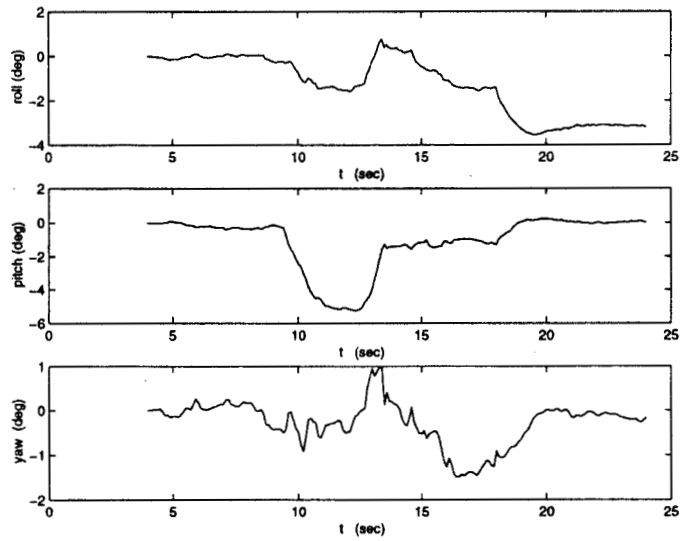


Figure 26: Estimate For Attitude

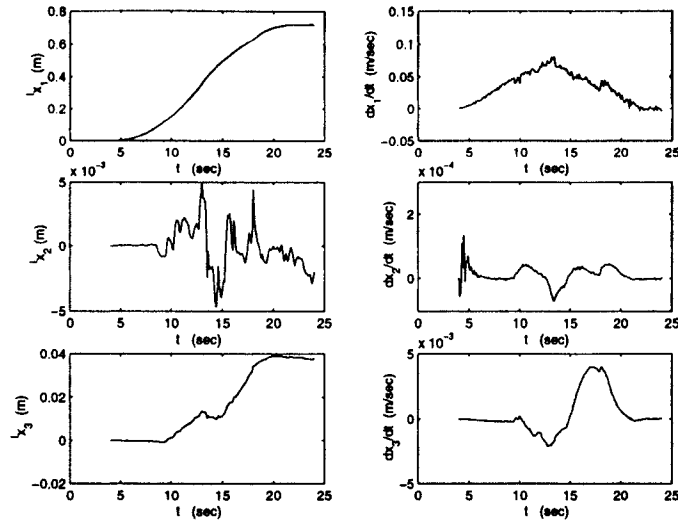


Figure 27: Estimate For Position and Velocities

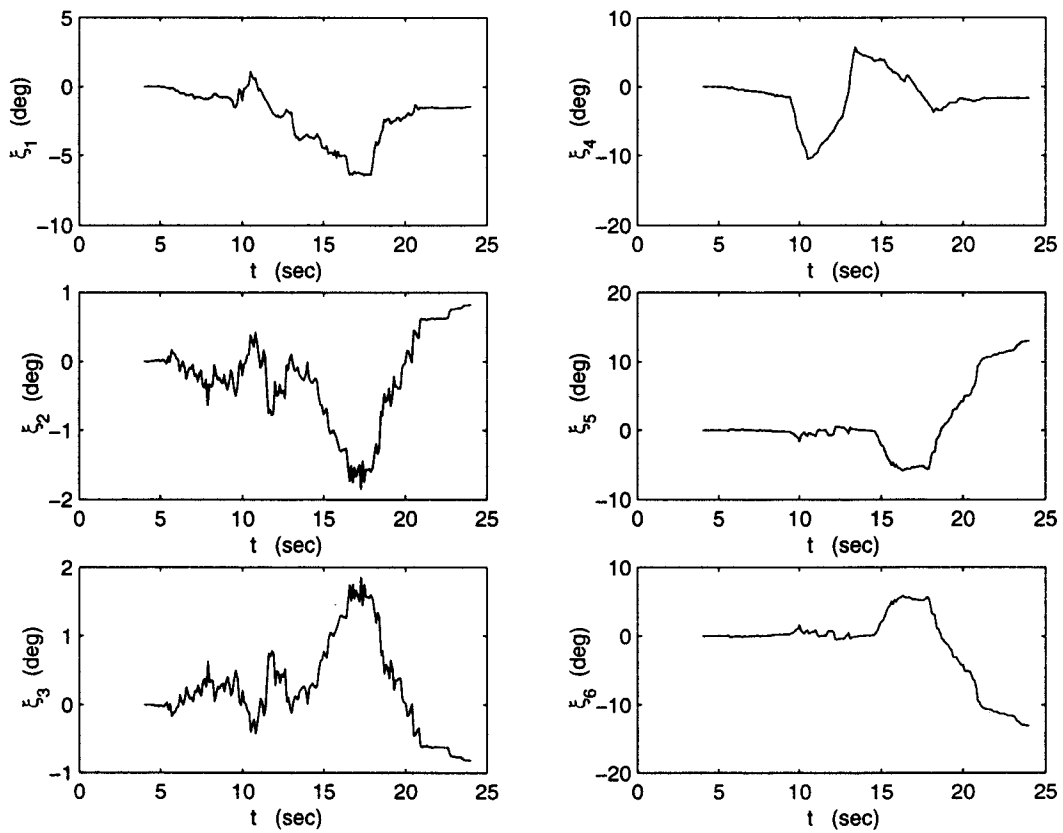


Figure 28: Estimate For Contact Angles

The corresponding covariances are shown in Figure 29 and Figure 30. An initial high covariance is reduced by the first few sensor measurements. As expected there is a growth of the positional covariance with time.

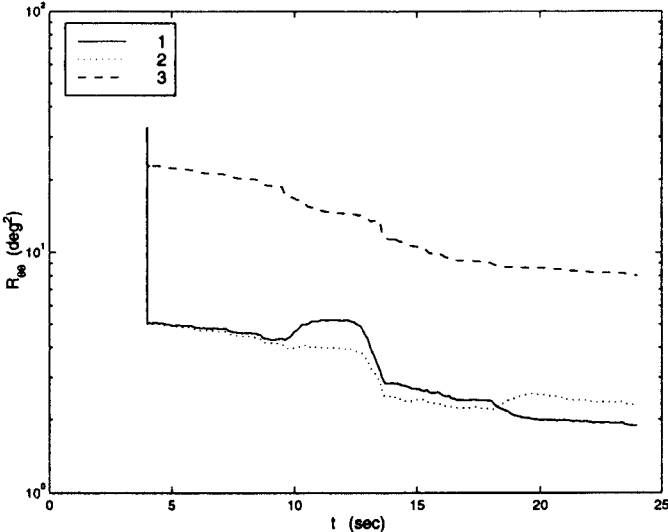


Figure 29: Covariance of Attitude Estimate In Terms of Small Angles

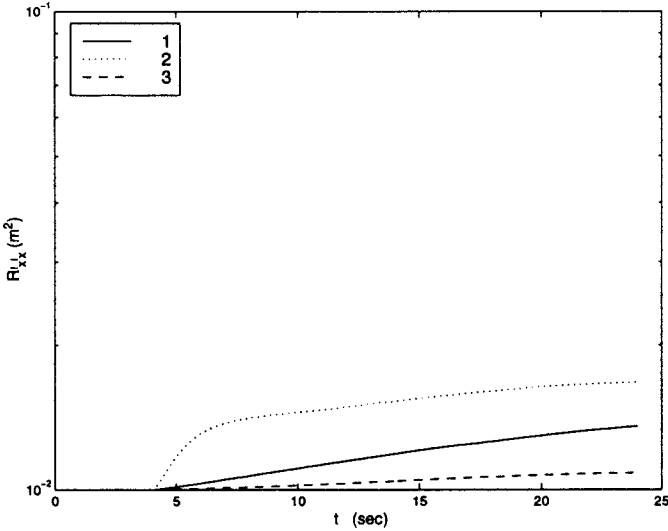


Figure 30: Covariance of Position Estimate

Ground-truth for this experiment is obtained by measuring tape and protractor at the end of the run. The estimated attitude values match the ground-truth values within the precision of the measurements taken. The estimated position values are within 1 cm of the ground-truth data and the estimated contact angles are within 5 degrees of the ground-truth.

## 5 Conclusion

We have demonstrated a kinematic estimator that successfully addresses the issues involved in roving a kinematically complex vehicle over non-flat terrain. By formulating a slip-measurement concept, we have been able to incorporate the kinematics and slip behavior of the vehicle into a Kalman filtering framework. In addition to more experiments to characterize and tune the system, we also expect to work on the following items:

- Incorporating the accelerometer sensor data during motion.
- Incorporating a smoother to post-process the sensor data every time the rover comes to one of its periodic halts. As we can obtain very precise attitude estimate when the rover is stopped using the accelerometer and sun-sensor, running the sensor data through the smoother will allow us to reconstruct many of the process disturbances and reduce the covariance of both the attitude and position estimates.
- Using some results from nonlinear observability theory that allows one to switch optimally between gyro and sun-sensor based attitude estimation together with simultaneous bias calibration of the gyro.
- Combining the kinematic estimator developed here with visual odometry and range-map matching techniques.

### Acknowledgments

This research was performed at the Jet Propulsion Laboratory, California Institute of Technology, under contract with the National Aeronautics and Space Administration.

## References

- [1] B. Barshan, and H.F. Durrant-Whyte, "Inertial navigation systems for mobile robots," *IEEE Transactions on Robotics and Automation*, Vol 11, No. 3, pp. 328-242, 1995.
- [2] E.T. Baumgartner and S.B. Skaar, "An autonomous vision-based mobile robot," *IEEE Transactions on Automatic Control*, 39(30), 493-502.
- [3] J. Borenstein and L. Feng, "Gyrodometry: A new method for combining data from gyros and odometry in mobile robots," *Proc. 1996 IEEE International Conference on Robotics and Automation*, pp. 423-428, Minneapolis, Minnesota, April 1996.
- [4] J. Fraden, *AIP Handbook of Modern Sensors: Physics, Designs, and Applications*, American Institute of Physics, New York, 1993.
- [5] Y. Fuke and E. Krotkov, "Dead Reckoning for a Lunar Rover on Uneven Terrain," *Proc. 1996 IEEE International Conference on Robotics and Automation*, pp. 411-416, Minneapolis, Minnesota, April 1996.
- [6] A. Gelb, ed., *Applied Optimal Estimation*, The M.I.T. Press, Cambridge, 1974.
- [7] P.C. Hughes, *Spacecraft Attitude Dynamics*. John Wiley & Sons, New York, 1986.
- [8] K.R. Kim, J.C. Lee and J.H. Kim, "Dead-reckoning for a Two-wheeled Mobile Robot on Curved Surfaces," *Proc. 1996 IEEE International Conference on Robotics and Automation*, pp. 1732-1737, Minneapolis, Minnesota, April 1996.
- [9] J.J. Leonard and H.F. Durrant-Whyte, "Mobile Robot Localization by Tracking Geometric Beacons," *IEEE Transaction on Robotics and Automation*, Vol 7, No. 3, pp. 376-382, 1991.
- [10] R. Madhavan, M.W.M.G. Dissanayake, and H.F. Durrant-Whyte, "Autonomous Underground Navigation of an LHD using a Combined ICP-EKF Approach," *Proc. 1998 IEEE International Conference on Robotics and Automation*, Leuven, Belgium, May 1998.
- [11] L. Matthies, *Dynamic Stereo Vision*, Ph.d. Thesis. Computer Science Department, Carnegie Mellon University, 1987.
- [12] L. Meirovich, *Methods of Analytical Dynamics*. McGraw-Hill, New York, 1970.
- [13] D.J. Montana, "The Kinematics of Contact and Grasp," *The International Journal of Robotics Research*, Vol. 7, No. 3, June 1988.
- [14] R.M. Murray, Z. Li and S.S. Sastry, *A Mathematical Introduction to Robotic Manipulation*, CRC Press, 1994.
- [15] C. Olson, "Mobile Robot Self-Localization by Iconic Matching of Range Maps," *Proc. of the 8th International Conference on Advanced Robotics*, pp. 447-452, 1997.

- [16] S. Roumeliotis and G. Bekey, "An Extended Kalman Filter for frequent local and infrequent global sensor data fusion," *Proc. SPIE Vol. 3209, 1997*.
- [17] J. Vaganay and M.J. Aldon, "Attitude Estimation For A Vehicle Using Inertial Sensors," *Control Eng. Practice*, Vol. 2, No. 2, pp. 281-287, 1994, Elsevier.
- [18] J. Yen, A. Jain and J. Balaram, "ROAMS : Rover Analysis, Modeling and Simulation Software," *Fifth International Symposium on Artificial Intelligence and Automation in Space*, Noordwijk, The Netherlands, 1-3 June 1999.